

Macro-micro mechanism of sand liquefaction under different waveforms via discrete element method (DEM)

Jiajin Zhao ^a, Zhehao Zhu ^{a,b,*}, Xiufeng Zhang ^c

^a School of Civil Engineering, Shanghai Normal University, Shanghai, 201418, China

^b Green and Intelligent Prevention Institute of Geological Disasters, Shanghai Normal University, Shanghai, 200234, China

^c Department of Geotechnical Engineering, Tongji University, Shanghai, 200092, China

ARTICLE INFO

Keywords:

Sand liquefaction
DEM
Cyclic triaxial test
Fabric characteristics
Anisotropy degree

ABSTRACT

Sand liquefaction is a critical geotechnical phenomenon in which saturated sand experiences a sudden loss of shear strength, resulting in various engineering failures. While past studies have extensively investigated liquefaction behaviour, the influence of waveform has received little attention. In particular, the connection between macroscopic mechanical behaviour and microscopic fabric evolution remains largely underexplored. To address this limitation, this study employed the Discrete Element Method (DEM) to simulate a series of undrained cyclic triaxial tests. The results revealed that rectangle waves caused the most severe liquefaction as a result of greater loading acting for a longer duration and produced unconventional liquefaction behaviours, as compared to sine and triangle waves. With coordination number (C_N) and the deviatoric part of the second invariant of the fabric tensor (J_2), this study demonstrates that both C_N and J_2 can effectively capture the liquefaction process. However, J_2 exhibited two distinct peaks at loading reversal points within the same cycle, expressing the inherent asymmetry in fabric anisotropy. A new indicator J_2^* was thus proposed to quantify the difference in peaks and a unified threshold value was identified, being a consistent marker for distinguishing liquefaction stages. Finally, a unified 3D liquefaction path was constructed integrating J_2 , stress ratio (η), and shear strain (ϵ_d). This unified framework provides deeper insights into the interplay between macromechanical response and microscopic fabric, offering a comprehensive perspective on liquefaction mechanism.

1. Introduction

Sand liquefaction is a devastating geotechnical phenomenon where saturated sand experiences a sudden loss of shear strength under dynamic loading, leading to large deformations and behaving as a liquid. As a result, this phenomenon has led to various spectacular engineering failures [1], such as bridge collapses in the 1999 Chi-Chi earthquake [2, 3], ground subsidence in the 2008 Wenchuan earthquake [4], clay flow in the 2018 Sulawesi earthquake [5,6], and landslides in the 2023 Jishishan earthquake [7]. These recurring disasters have posed significant challenges to the geotechnical community for performing advanced research into liquefaction mechanism [8,9].

Since the 1964 Alaska and Niigata earthquakes, cyclic triaxial tests have been extensively used to investigate the factors affecting liquefaction behaviours. Seed [10] introduced an equivalent method to substitute actual seismic recording with a sine wave. Subsequent studies have revealed the influence of soil properties such as saturation degree

[11,12], grain size distribution [13–15], void ratio [16], and initial anisotropy [17–22] on liquefaction potential. Regarding cyclic loading properties, considerable research has been devoted to examining the effects of adopted frequency and amplitude [23,24]. However, the widely adopted sine waves, characterised solely by a single component in the frequency domain, fall short of truly representing real seismic waves, which certainly exhibit complex superpositions of multiple harmonic components [25–28]. Recently, Zhu [25] designed a special experimental program with the consideration of three different waveforms (i.e., triangle, sine and rectangle waves) and discovered that rectangle waves caused a significantly higher liquefaction risk while maintaining the same cyclic stress ratio (CSR). This mechanism coexists with another mechanical aspect, in which the rapid loading reversal in rectangle waves is inherently linked to a very high loading rate [25,29]. Such conditions contribute to a greater resistance of sand specimens to deformation, in accordance with the conclusion drawn by Ishihara [30].

Relying on triaxial testing, the aforementioned studies succeeded in

* Corresponding author. School of Civil Engineering, Shanghai Normal University, Shanghai, 201418, China.

E-mail address: zhuzhehao@shnu.edu.cn (Z. Zhu).

establishing the cyclic strength curve based on the applied waveform. Yet, the concept of a triaxial specimen within a representative elementary volume serves merely as a macroscopic observation for describing sand liquefaction. For a triaxial specimen containing a vast number of grains, even state-of-the-art measurement techniques remain incapable of precisely recording microscopic evolution [31–37], such as grains arrangement and fabric anisotropy [31–37] that has been shown to significantly influence sand liquefaction [17,18,38–41].

For addressing fabric features, the discrete element method (DEM) has been widely adopted [42–46], offering a powerful numerical approach for simulating granular materials and enabling detailed analysis of fabric characteristics throughout the liquefaction process [47–49]. For instance, Gu et al. [31] identified a linear relationship between the coordination number and the effective mean principal stress at the critical state. Wang et al. [33] proposed the mean neighbouring particle distance (MNPD) to characterize the interparticle distance and further established a relationship between MNPD and the post-liquefaction shear strain. Otsubo et al. [32] revealed that the significant increase in fabric anisotropy during cyclic loading could serve as a pertinent precursor to soil skeleton collapse. They further proposed the concept of effective anisotropy to better explain the observed macroscopic behaviours. Ni et al. [50] demonstrated the suitability of DEM for analysing large post-liquefaction deformations, highlighting the direct correlation between axial strain evolution and fabric properties. Lv et al. [26] applied DEM to study the mechanical behaviour of soil-fibre mixtures under three waveforms, concluding that rectangle waves transferred higher energy to the soil skeleton. Meanwhile, the presence of fibres enhanced energy storage capacity, thereby mitigating dissipative strain energy. Despite the successful application of DEM in studying macroscopic and microscopic soil behaviours and their relation in between, research directly addressing the influence of different waveforms on liquefaction properties, particularly concerning the evolution of fabric characteristics, remains a paucity in the literature.

In order to overcome the above limitation, this study used the discrete element method (DEM) to investigate the effects of different waveforms on liquefaction behaviours under undrained triaxial conditions. Through the evolutions of excess pore water pressure and effective stress path, the distinct liquefaction development patterns were first clarified. Key fabric properties, such as coordination number and fabric tensor, were then adopted to establish the link between mechanical properties across micro and macro scales. Finally, a unified 3D liquefaction path was proposed to deepen the understanding of how anisotropy accumulation triggers sand liquefaction with the consideration of waveform.

2. Simulation methods

In this study, the discrete element software PFC6.0 was employed to conduct a series of constant volume cyclic triaxial tests, which has been widely recognised as an alternative for considering undrained behaviours [51,52]. To enhance computational efficiency, real particle morphology was simplified to spheres, and the particle size distribution was scaled up by 6.5 times, as shown in Fig. 1. To compensate for this oversimplification, the rolling resistance model was adopted. The model considers the rolling friction between non-spherical particles to effectively mimic their rolling characteristics during shearing [53–56]. The model parameters calibrated by Zhao et al. [36] for a commercially available reference sand (HN31) were adopted in this study, as listed in Table 1. To ensure consistency with the DEM framework, the maximum ($e_{\max} = 0.858$) and minimum void ratios ($e_{\min} = 0.619$) were also determined through DEM-based simulations following the procedure described in Ref. [57].

The DEM cubic specimens (5 cm × 5 cm × 5 cm) were generated with a void ratio e of 0.79 ($I_D = 0.28$), followed by the application of a consolidation pressure of 200 kPa until the specimen’s volume stabilised. The loading plates not only sealed the boundaries to maintain constant volume, but also directly applied effective stress to the specimens. A servo mechanism was employed to precisely control the applied stress by actively adjusting the position of the loading plates in response to feedback. Stress-controlled cyclic loading was then applied at a frequency of 0.1 Hz using sine, triangle, and rectangle waves, respectively. Seven cyclic stress ratios (CSR, the shear stress amplitude divided by the confining pressure) of 0.125, 0.15, 0.175, 0.20, 0.22, 0.25, and 0.262 were selected. To ensure phase consistency, all three waveforms included a half-cycle (5 s) of compression and extension. For sine and triangle waves, the loading reversal points were precisely synchronized for further analysis (see Fig. 2). In contrast, rectangle waves maintained a constant stress during each half-cycle, with the rapid transitions between compression and extension. Similar to experimental research, the

Table 1
DEM model parameters with rolling resistance model.

Linear Group		Particle-Particle	Particle-Facet
Effective Modulus	E^*	1.0E+08	1.0E+08
Normal-to-shear Stiffness Ratio	κ^*	2.0	2.0
Friction Coefficient	μ	0.43	0
Dashpot Group			
Normal critical damping ratio	β_n	0.20	0.20
Shear Critical Damping Ratio	β_s	0.20	0.20
Dashpot Mode	M_d	3	3
Rolling-Resistance Group			
Rolling Friction Coefficient	μ_r	0.20	0

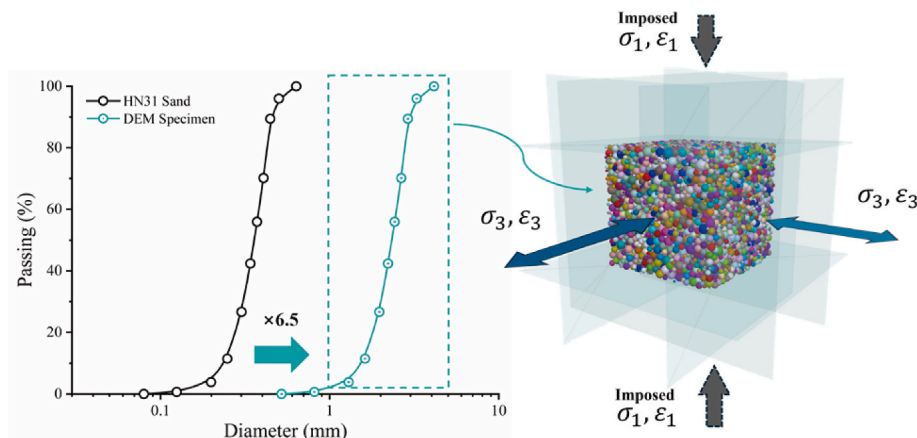


Fig. 1. Grain size distribution curve and DEM specimen.

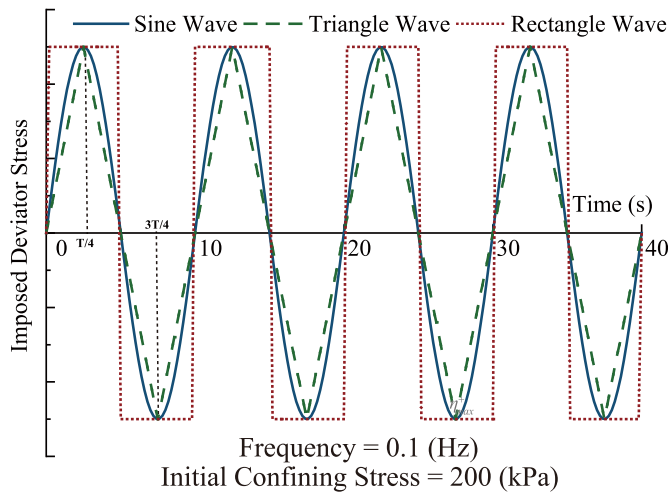


Fig. 2. Evolutions of imposed deviator stress in terms of time.

occurrence of 5 % double-amplitude (DA) axial strain [58,59] was set as the yardstick for recognising liquefaction onset.

3. Simulation results

3.1. Typical liquefaction behaviours

Fig. 3 displays the evolution of the excess pore water pressure ratio r_u ($r_u = \Delta u / \sigma'_c$) against the number of cycles N_{cyc} under three waveforms and different cyclic stress ratios CSRs. The graph shows that r_u gradually grew up as cyclic loading was applied. In the initial stage, the accumulation rates for three waveforms were nearly identical. However, as

N_{cyc} increased, the rectangle wave exhibited a much faster accumulation rate. Near liquefaction triggering, r_u steadily approached a value very close to 1.0. Regarding the impact of loading intensity, higher CSRs notably reduced the N_{cyc} needed to reach liquefaction. As for the impact of waveform, triangle waves required the highest N_{cyc} to reach $r_u = 0.90$ (see reference lines in Fig. 3), whilst rectangle waves required the fewest. The sine waves can be deemed to be the case in between. It is interesting to notice that the profiles for triangle and sine waves clearly exhibited a “double-peak” structure, whereas only “single-peak” structure was found for rectangle waves.

The effective stress paths of the DEM specimens subjected to different waveforms and CSRs are grouped in Fig. 4. All curves originated from the same point under the isotropic pressure of 200 kPa. With the progress of shearing, the effective stress paths continued to move toward the origin owing to the accumulation of excess pore water pressure (see Fig. 3). After passing through the phase transformation state (PTS), the DEM specimens experienced a slight dilatation, followed by a pronounced contraction upon the loading reversal. During the subsequent loading process, triangle and sine waves formed the so-called butterfly orbits along the Failure Line (FL), passing through the origin twice per cycle. This aligns with the “double-peak” structure in Fig. 3. In contrast, the butterfly orbits associated with rectangle waves passed through the origin only once per cycle, consistent with the “single-peak” structure shown in Fig. 3.

Fig. 5 displays the evolutions of axial strain ϵ_a as a function of N_{cyc} . As the cyclic loading was applied, ϵ_a exhibited only small oscillations, representing a quasi-elastic behaviour. With further loading, the amplitude of ϵ_a was sharply amplified. Based on the selected criterion of DA ϵ_a reaching 5 % (see solid markers in Fig. 5), the cyclic strength curves are plotted in Fig. 6. The graph shows that the three curves are clearly arranged from top to bottom as triangle, sine and rectangle waves, respectively. Combined with the observations in Figs. 3 and 4, it

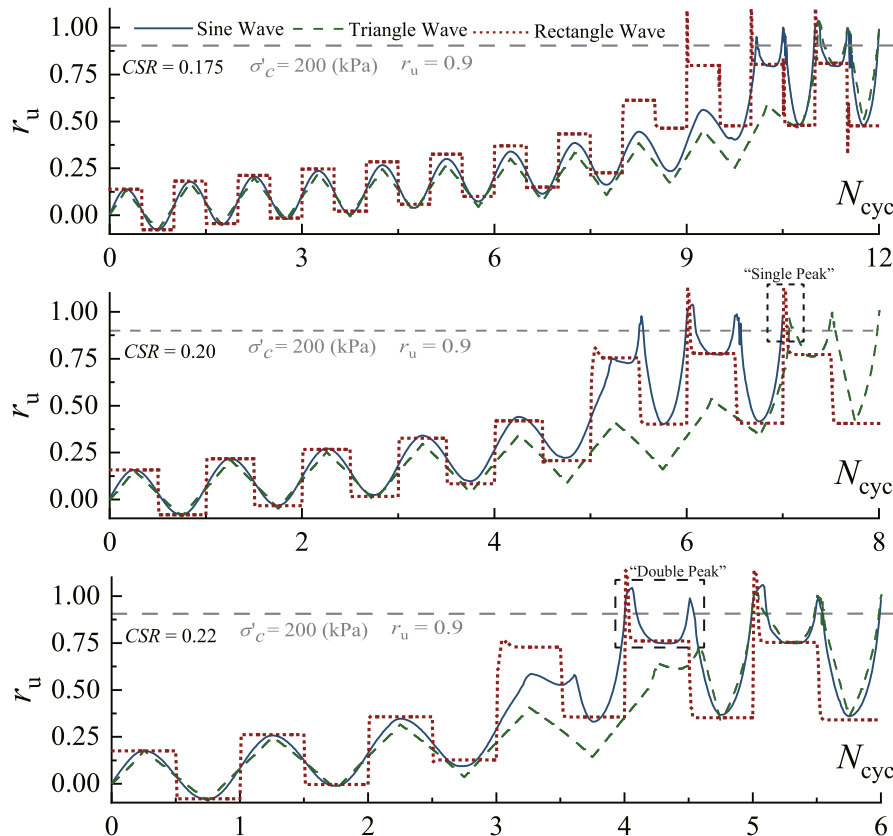


Fig. 3. Evolutions of excess pore water pressure ratio against number of cycles under different waveforms and CSRs.

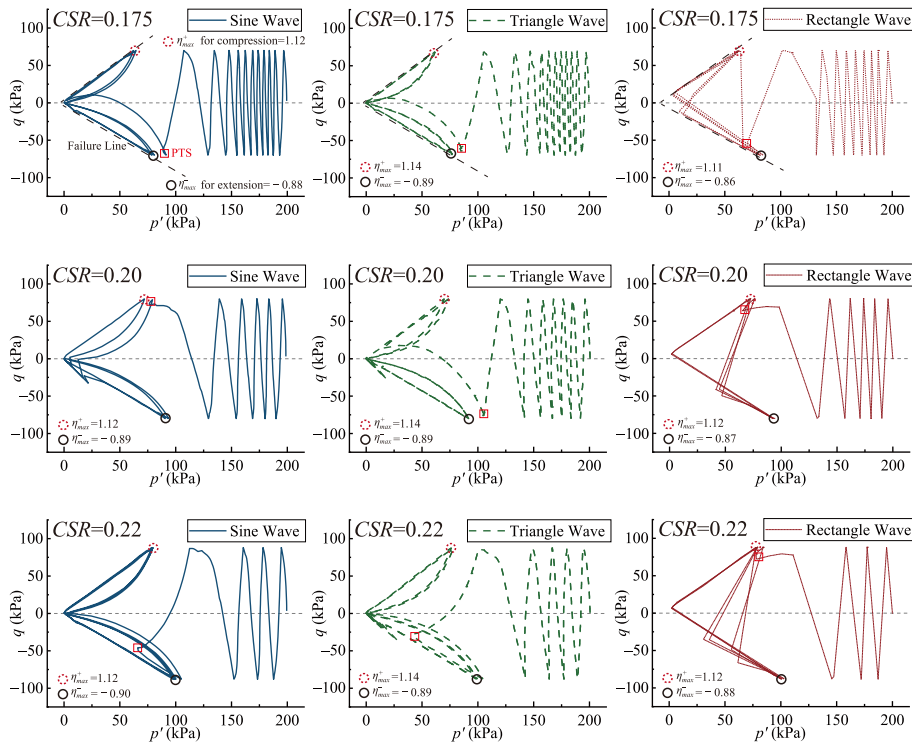


Fig. 4. Effective stress paths under different waveforms and CSRs.

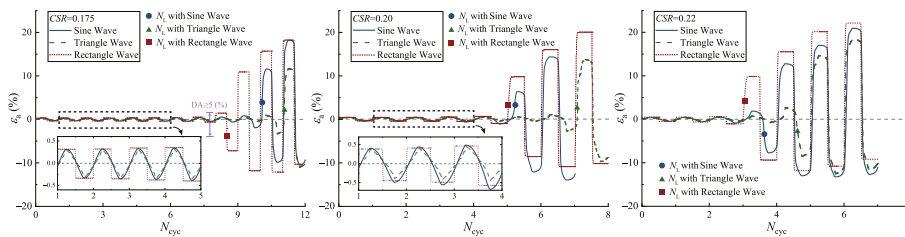


Fig. 5. Evolutions of axial strain against number of cycles under different waveforms and CSRs.

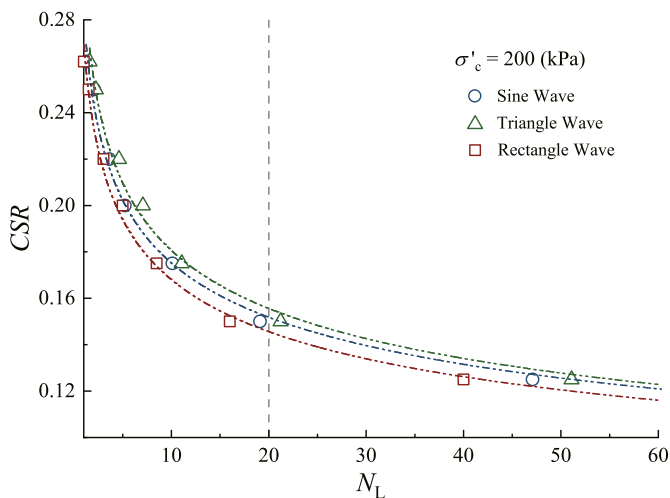


Fig. 6. Cyclic strength curve with $\sigma'_c = 200$ kPa.

can be now deduced that (i) rectangle and triangle waves induced the most and least severe liquefaction risk, with sine waves falling in between [25]; (ii) the liquefaction pattern induced by rectangle waves

distinguishes itself from the other two waveforms.

To highlight the unusual liquefaction responses induced by rectangle waves, a simulation result with $CSR = 0.22$ is discussed in detail, as depicted in Fig. 7. Several gauges points are put in the graph to help track changes. During the continuous dilatancy accumulation from point 1 (PTS) to point 2, the contractive potential of the specimen was notably enhanced [30]. In response to the instantaneous loading reversal from extension (point 2) to compression (point 3) in subplot (a), the specimen entered an immediate loading state. With the high contractive potential at point 2, sand liquefaction was finally triggered, resulting in the formation of a prominent peak on the excess pore water pressure curve. While maintaining a constant stress level (from point 3 to point 4), the excess pore water pressure remained almost constant. From compression (point 4) to extension (point 5), an instantaneous unloading was done in accordance with the rectangle wave. In contrast to the previous instantaneous loading phase (from point 2 to point 3), the confining pressure of the specimen decreased sharply, which theoretically promoted significant unloading contraction [30] due to the associated reduction in shear strength. Under the instantaneous unloading characteristic of the rectangle wave, the specimen lacked a sufficient time interval to fully develop its expected contractive deformation. As a result, the contraction was incomplete, preventing the occurrence of a second peak on the excess pore water pressure curve. For triangle and sine waves, the imposed stress varied in a gradual manner without time

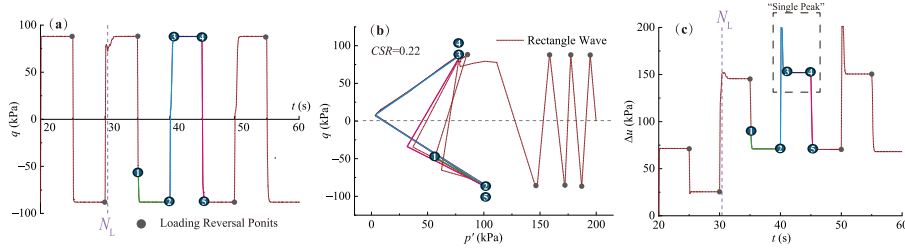


Fig. 7. Detailed responses near liquefaction with rectangle wave and CSR = 0.22: (a) imposed deviator stress (b) effective stress path (c) excess pore water pressure.

mismatch. Even under reversal loading with reducing confining pressure, the soil specimen still has a sufficient time interval to complete its deformation, resulting in the formation of a second peak. The above mechanism can logically explain how instantaneous reversals in rectangle waves produce the single-peak structure on the excess pore water pressure curve.

4. Microstructural characteristics during sand liquefaction

The interactions and contacts at the particle scale form the global bearing system capable of resisting external forces and generating pore water pressures. Consequently, the number of particle contacts and the degree of anisotropy serve as critical indicators for assessing liquefaction process. To bridge the microscopic characteristics and the relevant macroscopic behaviour with the consideration of different waveforms, this study selected two key microscopic quantities: (i) coordination number (C_N) and (ii) the deviatoric part of the second invariant of the fabric tensor (J_2). Both quantities are well established in previous research [33,36,50].

4.1. Evolution of coordination number and fabric tensor

The coordination number (C_N) is defined as the average number of contacts per particle. From a microscopic perspective, a higher C_N , in general, indicates a more robust force chain system, therefore contributing to a better shear resistance.

As shown in Fig. 8, the evolutions of C_N exhibited a similar trend under three waveforms. Before cyclic loading, the initial values of C_N were nearly equal at approximately 3 since the same initial state was assigned to all DEM specimens. With cyclic loading, C_N gradually

decreased with the increase in N_{cyc} , and the descending rate notably accelerated as the specimens approached $N_{cyc}/N_L = 1$ in Fig. 8. For different waveforms and CSRs, initial liquefaction (defined as DA ε_a reaching 5 %) consistently occurred for all specimens when C_N decreased to a narrow range of 2.3–2.5. At this stage, the particle assembly lost most of its interparticle contacts and transitioned into a “semi-suspended” state. When r_{li} increased to 1.0, all C_N values further decreased to approximately 1.0, implying that the bearing system was completely destroyed and the particle assembly exhibited a liquid-like response. In the post-liquefaction stage, C_N displayed periodic variations between 1.0 and 2.5 as the specimen underwent repeat cycles of strength degradation and recovery due to cyclic mobility.

According to the above, the development of sand liquefaction associated with the build-up of excess pore water pressure can be understood as the gradual loss of interparticle contacts at the microscopic scale. Despite the changes in CSR and waveform of the external loading, the microscopic responses in terms of C_N remains highly unified. The C_N values equalling to 2.5 and 1.0 correspond to the liquefaction criterion (i.e., DA $\varepsilon_a = 5.0$ %) and the initial occurrence (i.e., $r_{li} = 1.0$), respectively. Therefore, those two values can be considered as the intrinsic properties of granular materials, further independent of external loading conditions.

To investigate the anisotropy degree during sand liquefaction, the second-order contact normal fabric tensor (F_c) was used. The tensor can be defined following [60]:

$$F_c = \frac{1}{N_c} \sum_{k=1}^{N_c} v_c^k \otimes v_c^k \quad (1)$$

where N_c is the amount of particle contacts and v_c^k is the unit direction

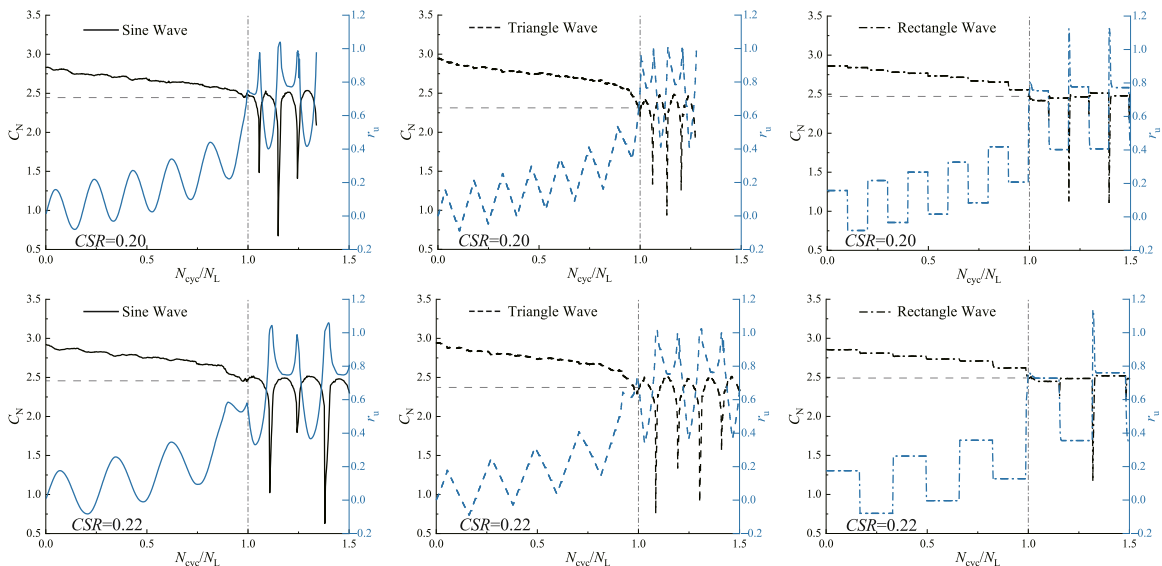


Fig. 8. Evolutions of coordination number and excess pore water pressure against normalized number of cycles under different waveforms.

vector pertaining to the k^{th} contact, respectively. Since F_c is a symmetric matrix, it can be decomposed into three eigenvalues (F_1, F_2 and $F_3 \in [0, 1]$). Given that v_c^k is a unit vector, the first invariant $I_1(F_c)$ is identically equal to 1 at all times. Therefore, the deviatoric part of the second invariant of the fabric tensor $J_2(F_c)$ can be expressed as:

$$\begin{cases} J_2(F_c) = \frac{1}{3}(I_1^2(F_c) - 3I_2(F_c)) = \frac{1}{3} - I_2(F_c) \\ I_1(F_c) = F_1 + F_2 + F_3 = 1 \\ I_2(F_c) = F_1F_2 + F_1F_3 + F_2F_3 \end{cases} \quad (2)$$

where the range of J_2 is from 0 to $\frac{1}{3}$. Analogy to the principal stress space, the three eigenvalues (i.e., F_1, F_2 and F_3) have been shown to span a principal fabric plane [36], in which J_2 reflects the anisotropy degree. When $J_2 = 1/3$, interparticle contacts are concentrated in a single direction, thus reaching the maximum anisotropy. Conversely, when $J_2 = 0$, interparticle contacts are uniformly distributed in all directions, resulting in the attainment of theoretical isotropy.

Fig. 9 displays the evolution of $\sqrt{J_2}$ under different waveforms. Prior to cyclic loading, all specimens were in the isotropic consolidated state with $\sqrt{J_2}$ very close to zero. After the initiation of cyclic loading, $\sqrt{J_2}$ began to periodically vary in response to the imposed deviator stress. With the increment in the loading amplitude, $\sqrt{J_2}$ exhibited an upward trend. It reached two different peaks (referred to as ‘‘C-peak’’ and ‘‘E-peak’’), corresponding to the loading reversal points in the compression and extension stages, respectively. Owing to the lower confining pressure during the extension stage, the specimen exhibited reduced shear strength and thus became more prone to deformation. This led to a stronger arrangement of oriented particles and a greater E-peak compared to the C-peak within the same cycle. In contrast, as loading amplitude decreased, the accumulated anisotropy gradually released and reached a minimal value when the imposed deviator stress was reduced to zero.

It is of great importance to notice that both the C-peak and E-peak values progressively rose as N_{cyc} increased, reflecting the gradual accumulation of fabric anisotropy during liquefaction process. While approaching liquefaction, the accumulation rate accelerated and finally reached a summit at the moment of liquefaction with $N_{\text{cyc}}/N_L = 1.0$. Following this, the specimens exhibited fluid-like isotropic properties, causing $\sqrt{J_2}$ to diminish in a sudden manner. During the cycles of strength degradation and recovery in the post-liquefaction stage, $\sqrt{J_2}$ also displayed a periodic pattern, closely resembling that observed for C_N in Fig. 8. The gap between C-peak and E-peak after liquefaction became smaller than that prior to liquefaction triggering, consistent with the observations in the accompanied study [36]. More importantly,

this study further proves that this phenomenon still holds true even when different waveforms are employed. As for the effect of waveforms, the curves depicted by $\sqrt{J_2}$ exhibited a clear ‘‘memory feature’’, with their outlines displaying a strong resemblance to the imposed waveforms governed by both q and σ_c . This suggests the existence of a correlation between fabric properties and mechanical indicators, which will be discussed in detail in the next section.

Fig. 10 displays the threshold values of $\sqrt{J_2}$ at liquefaction (i.e., $N_{\text{cyc}}/N_L = 1.0$) as a function of CSR. The graph contains the results of all simulations, covering three waveforms and seven CSRs. Despite CSR varying between 0.125 and 0.262 and waveform altering from triangle to rectangle, the scatter points remain closely aligned with the same fitting line. This indicates that, although the cyclic strength curve at the macroscopic scale indeed changes with waveforms (see Fig. 6), the liquefaction mechanism in terms of fabric anisotropy at the microscopic scale is unique. Different waveforms are more likely to significantly change the build-up of excess pore water pressure and thereby create their own cyclic strength curve (see Fig. 3). However, the anisotropic threshold is independent of external loading conditions and is solely determined by the initial soil structure, reconfirming that it is an intrinsic property of granular materials, in agreement with the conclusion for C_N .

4.2. Evolution of anisotropy at loading reversal points

As justified in Fig. 9 that fabric anisotropy exhibits two distinct peaks

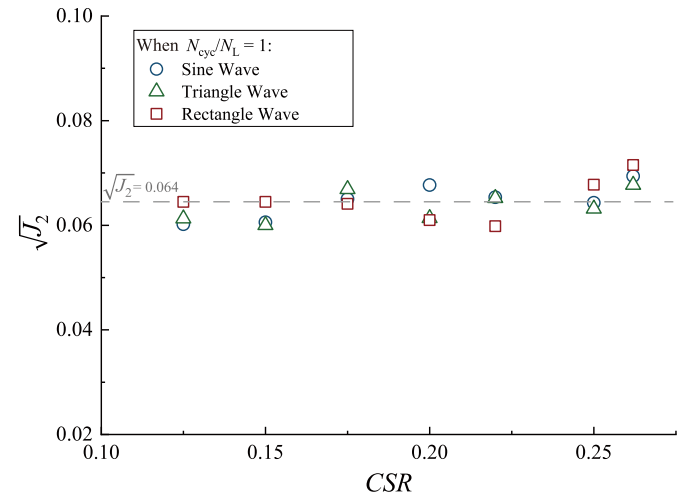


Fig. 10. Square root of $J_2(F_c)$ at $N_L/N_{\text{cyc}} = 1.0$ for initial liquefaction.

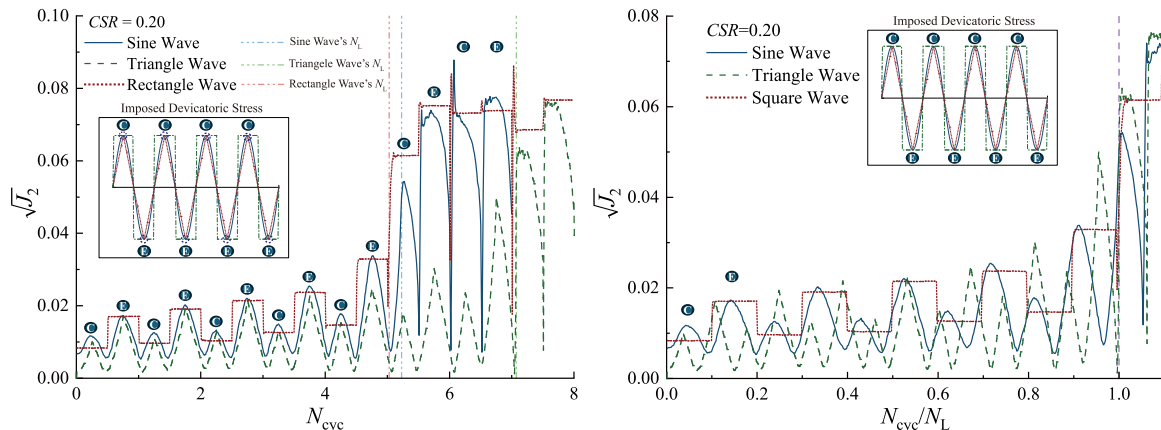


Fig. 9. Evolutions of $\sqrt{J_2}$ against number of cycles and normalized number of cycles under different waveforms.

(referred to as C-peak and E-peak) at the loading reversal points within each cycle, the evolutions of these peaks are summarized in Fig. 11. Both curves can be fitted with a Sigmoid function in a high confidence interval, as fabric anisotropy displayed minimal growth in the early stage but significantly increased as liquefaction approached. This conforms to the characteristic trend determined by the Sigmoid function. In spite of the different waveforms, C-peak and E-peak form two unified curves. Therefore, it can be inferred that the anisotropic property during the compression and extension phases across different stages of liquefaction equally reflects an inherent property determined by the initial soil structure. With the progress in liquefaction, the difference between C-peak and E-peak decreased with N_{cyc}/N_L . To directly quantify this change, a new indicator J_2^R is defined in Fig. 12 as follows:

$$J_2^R = \frac{\sqrt{J_2^C}}{\sqrt{J_2^E}} \quad (3)$$

where J_2^C and J_2^E represent the value of C-peak and E-peak, respectively. J_2^R is constrained to a maximum value of 1 because J_2^E is greater than J_2^C . It can be observed in Fig. 12 that (i) most points before the liquefaction onset are concentrated in the bottom left part; (ii) after liquefaction onset, the majority of points shifts to the upper right part; (iii) J_2^R equalling to 0.7 delineates the boundary between pre- and post-liquefaction phases. In addition to the fabric anisotropies themselves at the loading reversals points, their difference within the same cycle also effectively reflects the development of sand liquefaction. It is essential to mention that while the coordination number C_N strongly maps the evolution of excess pore water pressure Δu (see Fig. 8), its definition limit the ability to capture any asymmetry of anisotropy at loading reversals points, which is very important in understanding liquefaction process. With this consideration, fabric anisotropy is adopted hereinafter to construct a three-dimensional macro-micro liquefaction path.

4.3. Three-dimensional liquefaction path

Within the framework of critical state soil mechanics, the stress ratio η ($\eta = q/p'$) and shear strain ϵ_d ($\epsilon_d = 1.5 \times \epsilon_a$ in undrained conditions) describe the mechanical response of sand under cyclic loading. Fig. 13 depicts the relationship between η and ϵ_d at the loading reversal points. During both the compression and extension phases, the stress ratio and shear strain form a unified curve. Starting from the origin ($\eta = 0$), the stress ratio rapidly increased with small shear strain. As cyclic loading progressed, the specimens produced greater deformation to sustain the

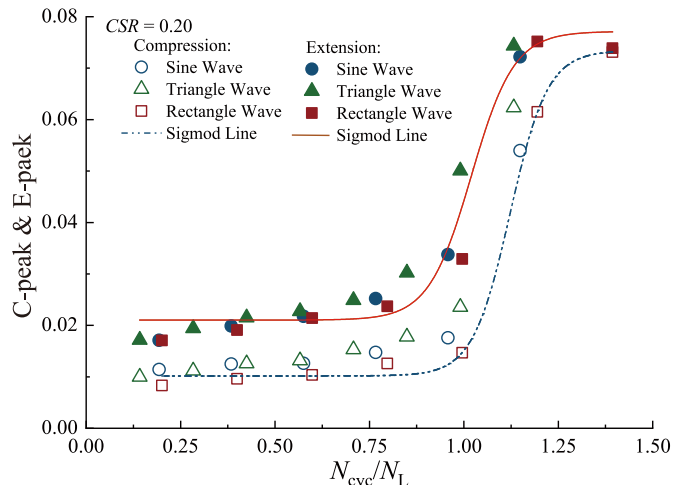


Fig. 11. Evolutions of C-peak and E-peak against normalized number of cycles.

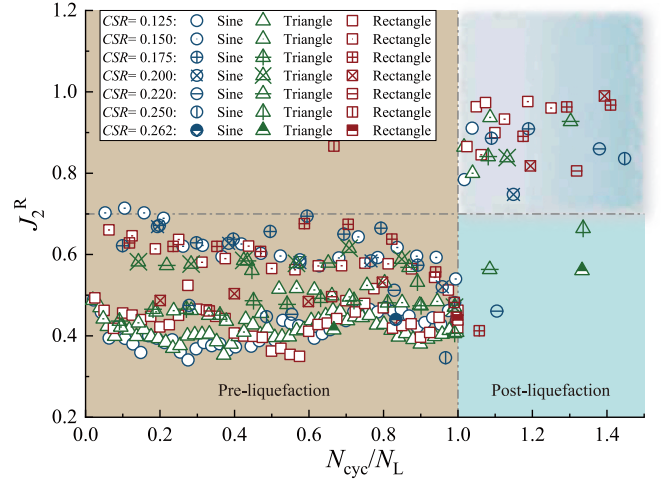


Fig. 12. Distribution of J_2^R under different waveforms and CSRs.

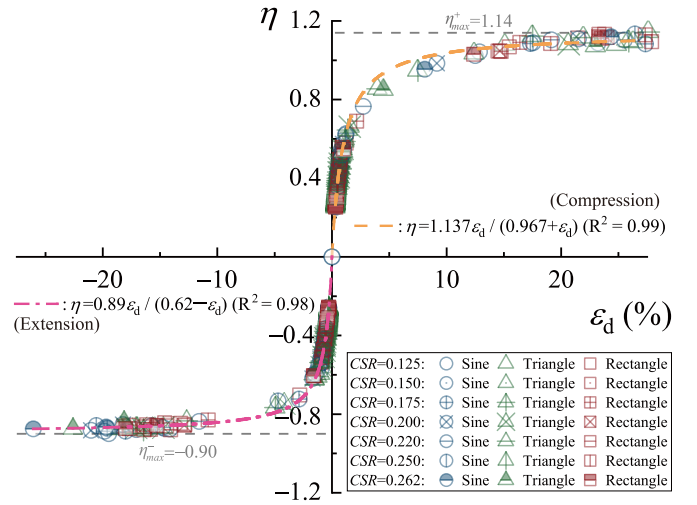


Fig. 13. Relationship between the stress ratio and shear strain at loading reversal points.

same level of external loading. As the absolute value of ϵ_d approached 3.3 % (corresponding to the adopted liquefaction failure with DA ϵ_a equalling to 5.0 %), two curves flattened with η gradually stabilizing toward their respective asymptotes. These values correspond to the Failure Line (FL) in Fig. 4, representing the failure state of the specimen. Due to the asymmetry in stress-strain responses between compression and extension, the fitting functions and FL differ between the two phases. However, they remain continuous at the origin, ensuring a smooth transition. For DEM specimens sharing the same initial structure, the relationship between η and ϵ_d remains unchanged, regardless of variations in CSR and waveform.

Fig. 14 illustrates the relationship between $\sqrt{J_2}$ and η at all reversal points. The results show a clear functional relationship between fabric anisotropy and stress ratio. As the absolute value of η increases, J_2 exhibits a monotonic rise. And the exponential-based fitted functions still satisfy the continuity at the origin. When η approach the FL (i.e., η_{max} and η_{min}^+), J_2 ceases to evolve and settles around the endpoints of the curve. Similar to the earlier cases, the macro-micro relationship in Fig. 14 remains independent with any variations in loading intensity or waveform. Therefore, with η , ϵ_d and $\sqrt{J_2}$ are adopted, a 3D plane integrating both microscopic fabric properties and macroscopic mechanical responses can be established. In soil mechanics, (i) η is a crucial indicator

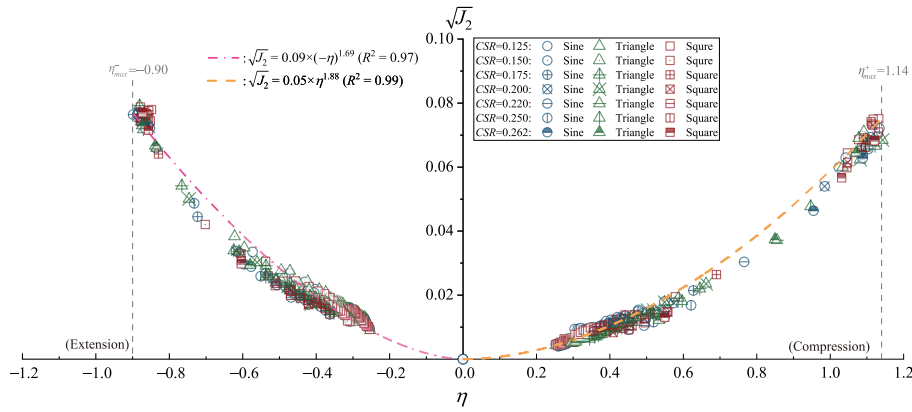


Fig. 14. Relationship between $\sqrt{J_2}$ and stress ratio at loading reversal points.

within the framework of critical state theory to characterize the failure behaviour under complex stress conditions; (ii) ϵ_d is capable of mapping the nonlinear stress-strain relationship and dynamics properties of soils [30,50]. The connection between the above two indicators and $\sqrt{J_2}$ should provide a deep insight into the interplay across different scales and enables more accurate description of sand liquefaction while

considering various loading scenarios including different waveforms.

Fig. 15a presents a three-dimensional coordinate system containing the simulation results with $CSR = 0.20$. The corresponding loading reversal points are circled in the graph. Despite different waveforms, the points basically fall on the same curve, which is the liquefaction path proposed in this study. Following this logic, Fig. 15b summarizes the

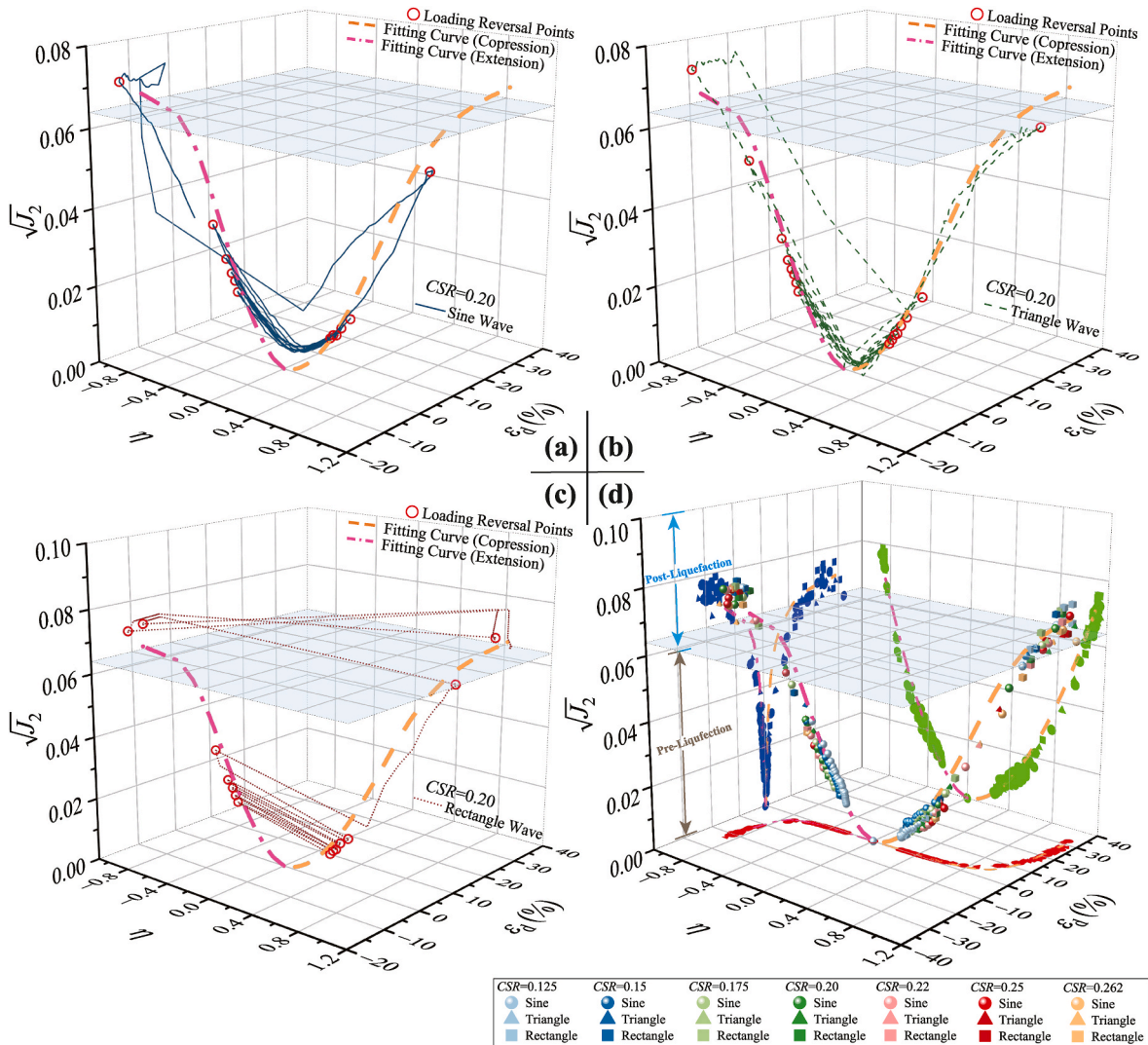


Fig. 15. Relationship between J_2 , stress ratio η and shear strain ϵ_d under $CSR = 0.20$ at loading reversal points: (a) sine wave; (b) triangle wave; (c) rectangle wave; (d) 3D liquefaction paths of all specimens.

loading reversals points across all simulations results. A unified “funnel-shaped” path can be formed, containing both the compression ($\eta \geq 0$ and $\varepsilon_d \geq 0$) and extension ($\eta \leq 0$ and $\varepsilon_d \leq 0$) stages. This observation reinforces the idea that the relationship between soil microstructure and macroscopic responses such as stress ratio and shear strain is an inherent property of the initial soil structure, rather than the specifics of the applied loading waveform or intensity. The path can be fitted using the following functions to guarantee the continuity at the origin:

$$\begin{cases} 0.058 \times \eta^{2.885} - \frac{1.137 \times \varepsilon_d \times \sqrt{J_2}}{0.967 + \varepsilon_d} = 0 (\eta \geq 0) \\ 0.09 \times (-\eta)^{2.69} - \frac{0.89 \times \varepsilon_d \times \sqrt{J_2}}{0.62 - \varepsilon_d} = 0 (\eta \leq 0) \end{cases} \quad (4)$$

In fact, the 3D liquefaction path can be reduced in dimensionality and projected onto two orthogonal planes, thus producing Figs. 13 and 14 discussed earlier. There exists a threshold plane with $\sqrt{J_2} = 0.064$ (see Fig. 10) separating the space into two regions: (i) the lower half with $\sqrt{J_2} < 0.064$ corresponds to the pre-liquefaction stage; (ii) the upper half with $\sqrt{J_2} > 0.064$ corresponds to the post-liquefaction stage.

For better visualization, a conceptual schematic is highlighted in Fig. 16. Before applying deviator stress, the liquefaction path is located at the origin (Point 0). After the beginning of cyclic loading, the liquefaction path ascends along the backbone curve to a C-peak (Point 1) in the compression stage. Upon loading reversal, the liquefaction path descends to zero before ascending again to a E-peak (Point 2) in the extension phase. Under the repeated action of loading reversal, the liquefaction path oscillates along the backbone curve like a pendulum. However, the path is asymmetric on the compression and extension sides because E-peak is generally more important than C-peak as previously discussed. With further loading, the C-peak and E-peak yielded within each cycle become greater than those pertaining to the former cycle and finally surpass the anisotropic threshold triggering sand liquefaction (Point 4). The specimen suddenly exhibits fluid-like isotropic characteristic, causing the liquefaction path to return to zero as the difference between C-peak and E-peak diminishes.

For special rectangle waves, the liquefaction path slightly differs due to their instantaneous loading and unloading. As a result, the liquefaction path jumps between the loading reversal points at the compression and extension phases, instead of closely following the backbone curve (see Fig. 15a). Although the liquefaction responses induced by rectangle

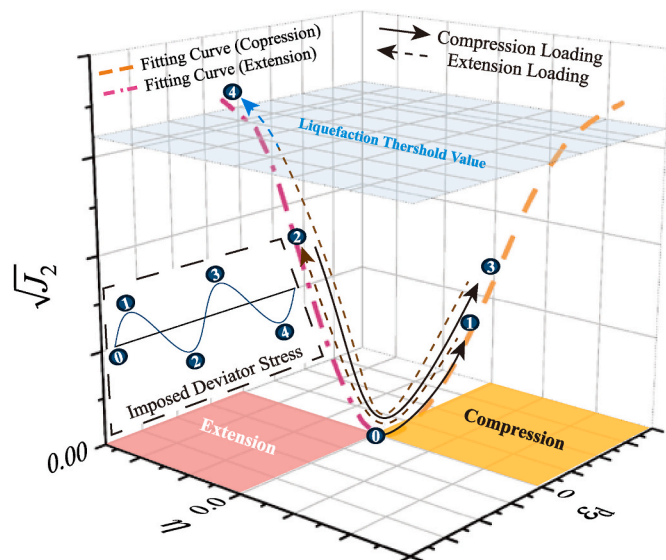


Fig. 16. Schematic of sand liquefaction path integrating macroscopic (η , ε_d) and microscopic quantities (J_2).

waves are quite special due to their instantaneous stress reversals, the corresponding liquefaction mechanism across macro and micro scales remains unified as long as the initial soil structure is defined.

In general, establishing the relationship between stress ratio and shear strain in conventional constitutive models often requires many fitting parameters. Some parameters are typically determined through a subjective trial-and-error procedure, such as the fabric-dilatancy parameter in Bounding Surface Model [61]. Such dependency significantly impedes the practical application and broader adoption of constitutive models in engineering practice. By contrast, the findings of this study support the development of microstructure-informed formulations that can directly describe complex macroscopic behaviours. This advancement has great potential to facilitate the construction of constitutive models rooted in microscale physics, enabling a more intrinsic representation of the mechanical behaviour of granular materials by directly considering their internal structure and interaction mechanisms. It should be noted that, due to the inherent boundary limitations of conventional triaxial tests, the principal stress directions remain fixed during loading. As a result, while this study focuses on fabric evolution under controlled stress paths, it does not encompass the additional complexity introduced by principal stress rotation. Previous studies [62–64] have demonstrated that such rotation might probably influence particle rearrangement and fabric development. Therefore, further studies are needed to extend the current micro-scale framework to more generalized loading conditions involving stress path rotation.

5. Conclusions

This study employed the Discrete Element Method (DEM) to simulate undrained triaxial shear tests under three different waveforms (sine wave, triangle wave and rectangle wave) and seven cyclic stress ratios ($CSR = 0.125, 0.15, 0.175, 0.20, 0.22, 0.25$ and 0.262). Through the evolutions of (i) excess pore water pressure, (ii) effective stress path and (iii) axial strain, the mechanical behaviour was first investigated. The coordination number (C_N) and the deviatoric part of the second invariant of the fabric tensor (J_2) were then adopted as microscopic indicators to capture interparticle contacts and fabric anisotropy, respectively. Due to the compression-extension asymmetry, a new indicator J_2^R was proposed to quantify the difference in fabric anisotropy at loading reversal points. Finally, a unified macro-micro 3D conceptual model integrating stress ratio, shear strain and fabric anisotropy was established. The following conclusions can be drawn:

1. Under the same CSR , rectangle wave requires the fewest cycles to trigger initial liquefaction, followed by sine and triangle waves. The influence of waveform on mechanical behaviour is primarily reflected in the shape of the excess pore water pressure curves.
2. C_N and J_2 exhibit threshold values for the liquefaction triggering. These thresholds can be considered to be the intrinsic properties of the material.
3. The proposed J_2^R effectively captures the anisotropy difference at the loading reversal points. For the DEM specimens involved in this study, J_2^R equalling to 0.7 delineates the boundary between pre- and post-liquefaction phases.
4. The liquefaction path oscillates along a unified 3D “funnel-shaped” curve, accumulating fabric anisotropy in a gradual manner with external loading. This finding provides a unified framework for describing liquefaction phenomenon across different scales.

CRedit authorship contribution statement

Jiajin Zhao: Writing – original draft, Visualization, Validation, Methodology, Investigation, Formal analysis, Data curation, Conceptualization. **Zhehao Zhu:** Writing – review & editing, Supervision, Resources, Project administration, Funding acquisition. **Xiufeng Zhang:**

Software.

Declaration of competing interest

The authors declare that they have no known competing financial interests or personal relationships that could have appeared to influence the work reported in this paper.

Acknowledgments

The financial support provided by the National Natural Science Foundation of China (Grant No. 42307190) is deeply acknowledged.

Data availability

Data will be made available on request.

References

- Ishihara K. Liquefaction-induced flow slide in the collapsible loess deposit in Soviet Tajik. *Soils Found* 1990;30:73–89. <https://doi.org/10.3208/SANDF1972.30.4.73>.
- Wang TT, Kwok OLA, Jeng FS. Seismic response of tunnels revealed in two decades following the 1999 Chi-Chi earthquake (Mw 7.6) in Taiwan: a review. *Eng Geol* 2021;287:106090. <https://doi.org/10.1016/j.enggeo.2021.106090>.
- Qi H, Zhou J, Peng K, Khandelwal M. Knowledge structure and research progress in earthquake-induced liquefaction assessment from 2000 to 2023: a scientometric analysis incorporating domain knowledge. *Soil Dynam Earthq Eng* 2025;188: 109075. <https://doi.org/10.1016/j.soildyn.2024.109075>.
- Huang Y, Jiang X. Field-observed phenomena of seismic liquefaction and subsidence during the 2008 Wenchuan earthquake in China. *Nat Hazards* 2010;54: 839–50. <https://doi.org/10.1007/S11069-010-9509-6>.
- Kiyota T, Shiga M, Mori K, Katagiri T, Furuichi H, Setiawan H. Triggering mechanism of long-distance flow-type landslides caused by 2018 Sulawesi Earthquake, Indonesia. *Soils Found* 2025;65:101544. <https://doi.org/10.1016/j.sandf.2024.101544>.
- Hazarika H, Rohit D, Pasha SMK, Maeda T, Masyhur I, Arsyad A, et al. Large distance flow-slide at jono-oge due to the 2018 Sulawesi earthquake, Indonesia. *Soils Found* 2021;61:239–55. <https://doi.org/10.1016/j.sandf.2020.10.007>.
- Xiao S, Zhang L, He J, Peng M, Jiang R, Lu W. Hypermobility of a catastrophic earthquake-induced loess landslide. *Eng Geol* 2024;343:107777. <https://doi.org/10.1016/j.enggeo.2024.107777>.
- Seed HB, Idriss IM. Analysis of soil liquefaction: Niigata earthquake. *J Soil Mech Found Div* 1967;93:83–108. <https://doi.org/10.1061/JSFEAQ.0000981>.
- Seed HB, Lee KL. Liquefaction of saturated sands during cyclic loading. *J Soil Mech Found Div* 1966;92:105–34. <https://doi.org/10.1061/JSFEAQ.0000913>.
- Seed HB. Representation of irregular stress time histories by equivalent uniform stress series in liquefaction analyses, vol 75. College of Engineering, University of California; 1975.
- Ishihara K, Yasuda S, Nagase H. Soil characteristics and ground damage. *Soils Found* 1996;109–18. <https://doi.org/10.3208/SANDF.36.SPECIAL.109>.
- Ishihara K. Liquefaction and flow failure during earthquakes. *Geotechnique* 1993; 43:351–451. <https://doi.org/10.1680/GEOT.1993.43.3.351>.
- Sadrekarimi A. Influence of fines content on liquefied strength of silty sands. *Soil Dynam Earthq Eng* 2013;55:108–19. <https://doi.org/10.1016/j.soildyn.2013.09.008>.
- Zhao J, Zhu Z, Liu J, Zhong H. Damping ratio of sand containing fine particles in cyclic triaxial liquefaction tests. *Appl Sci* 2023;13:4833. <https://doi.org/10.3390/AP13084833>.
- Soares M, Viana Da Fonseca A. Factors affecting steady state locus in triaxial tests. *Geotech Test J* 2016;39:1056–78. <https://doi.org/10.1520/GTJ20150228>.
- Molina-Gómez F, González-Olaya R, Camacho-Tauta J. Exploring liquefaction resistance in saturated and gassy sands at different state parameters. *Transp Geotech* 2024;49:101410. <https://doi.org/10.1016/j.trgeo.2024.101410>.
- Yamashita S, Toki S. Effects of fabric anisotropy of sand on cyclic undrained triaxial and torsional strengths. *Soils Found* 1993;33:92–104. <https://doi.org/10.3208/SANDF1972.33.3.92>.
- Morimoto T, Otsubo M, Koseki J. Microscopic investigation into liquefaction resistance of pre-sheared sand: effects of particle shape and initial anisotropy. *Soils Found* 2021;61:335–51. <https://doi.org/10.1016/j.sandf.2020.12.008>.
- Ye B, Ni X, Ye G, Huang Y, Lu P. Prediction of the initial point of the last cycle in undrained cyclic triaxial tests on flow liquefaction. *Soil Dynam Earthq Eng* 2019; 120:12–22. <https://doi.org/10.1016/j.soildyn.2019.01.028>.
- Ni X, Ye B, Zhang F, Feng X. Influence of specimen preparation on the liquefaction behaviors of sand and its mesoscopic explanation. *J Geotech Geoenviron Eng* 2021; 147:04020161. [https://doi.org/10.1061/\(ASCE\)GT.1943-5606.0002456](https://doi.org/10.1061/(ASCE)GT.1943-5606.0002456).
- Hidayat RF, Kiyota T, Umar M, Rosiyani Nawir H. Flow deformation characteristics of sandy soils under constant shear stress with water inflow. *Soils Found* 2022;62. <https://doi.org/10.1016/j.sandf.2022.101128>.
- Zhuang H, Wang R, Chen G, Miao Y, Zhao K. Shear modulus reduction of saturated sand under large liquefaction-induced deformation in cyclic torsional shear tests. *Eng Geol* 2018;240:110–22. <https://doi.org/10.1016/j.enggeo.2018.04.018>.
- Zhu Z, Zhang F, Peng Q, Dupla JC, Canou J, Cumunel G, et al. Effect of the loading frequency on the sand liquefaction behaviour in cyclic triaxial tests. *Soil Dynam Earthq Eng* 2021;147. <https://doi.org/10.1016/j.soildyn.2021.106779>.
- Ni X, Ye B, Cheng Z, Ye G. Evaluation of the effects of initial deviatoric stress and cyclic stress amplitude on liquefaction potential of loose and medium-dense sands: an energy-based method. *Soil Dynam Earthq Eng* 2020;136:106236. <https://doi.org/10.1016/j.soildyn.2020.106236>.
- Zhu Z, Zhang F, Peng Q, Dupla JC, Canou J, Cumunel G, et al. Assessment of the loading waveform on the cyclic liquefaction resistance with Hostun 31 sand. *Soil Dynam Earthq Eng* 2021;150:106919. <https://doi.org/10.1016/j.soildyn.2021.106919>.
- Comput Geotech 2022;151:104961. <https://doi.org/10.1016/j.compgeo.2022.104961>.
- Shinji S, Hiroyuki Y. Simplified liquefaction prediction and assessment method considering waveforms and durations of earthquakes. *J Geotech Geoenviron Eng* 2017;143:04016091. [https://doi.org/10.1061/\(ASCE\)GT.1943-5606.0001597](https://doi.org/10.1061/(ASCE)GT.1943-5606.0001597).
- Jiang M, Kamura A, Kazama M. Comparison of liquefaction behavior of granular material under SH- and Love-wave strain conditions by 3D DEM. *Soils Found* 2021; 61:1235–50. <https://doi.org/10.1016/j.sandf.2021.06.013>.
- Miao Y-H, Sheng R-Y, Yin J, Zhou F-B, Lu J-F. Dynamic characteristics of saturated soft clays under cyclic loading in drained condition. *KSCSE J Civ Eng* 2020;24: 443–50. <https://doi.org/10.1007/s12205-020-1539-3>.
- Ishihara K. Soil behaviour in earthquake geotechnics. Oxford University Press; 1996. <https://doi.org/10.1093/oso/9780198562245.001.0001>.
- Gu X, Huang M, Qian J. DEM investigation on the evolution of microstructure in granular soils under shearing. *Granul Matter* 2014;16:91–106. <https://doi.org/10.1007/s10035-013-0467-z>.
- Otsubo M, Chitravel S, Kuwano R, Hanley KJ, Kyokawa H, Koseki J. Linking inherent anisotropy with liquefaction phenomena of granular materials by means of DEM analysis. *Soils Found* 2022;62:101202. <https://doi.org/10.1016/j.sandf.2022.101202>.
- Wang R, Fu P, Zhang JM, Dafalias YF. DEM study of fabric features governing undrained post-liquefaction shear deformation of sand. *Acta Geotech* 2016;11: 1321–37. <https://doi.org/10.1007/S11440-016-0499-8>.
- Gu X, Zhang J, Huang X. DEM analysis of monotonic and cyclic behaviors of sand based on critical state soil mechanics framework. *Comput Geotech* 2020;128: 103787. <https://doi.org/10.1016/j.compgeo.2020.103787>.
- Nie Z, Qi Q, Wang X, Zhu Y. DEM investigation of strain behaviour and force chain evolution of gravel-sand mixtures subjected to cyclic loading. *Particulate* 2022; 68:13–28. <https://doi.org/10.1016/j.partic.2021.10.006>.
- Zhao J, Zhu Z, Zhang D, Wang H, Li X. Assessment of fabric characteristics with the development of sand liquefaction in cyclic triaxial tests: a DEM study. *Soil Dynam Earthq Eng* 2024;176:108343. <https://doi.org/10.1016/j.soildyn.2023.108343>.
- Oda M. Initial fabrics and their relations to mechanical properties of granular material. *Soils Found* 1972;12:17–36. <https://doi.org/10.3208/sandf1960.12.17>.
- Le NB, Toyota H, Takada S. Evaluation of mechanical properties of mica-mixed sand considering inherent anisotropy. *Soils Found* 2020;60:533–50. <https://doi.org/10.1016/j.sandf.2020.04.003>.
- Song LX, F DY. Anisotropic critical state theory: role of fabric. *J Eng Mech* 2012; 138:263–75. [https://doi.org/10.1061/\(ASCE\)EM.1943-7889.0000324](https://doi.org/10.1061/(ASCE)EM.1943-7889.0000324).
- Miura S, Toki S. Anisotropy in mechanical properties and its simulation of sands sampled from natural deposits. *Soils Found* 1984;24:69–84. <https://doi.org/10.3208/SANDF1972.24.3.69>.
- Ladd RS. Specimen preparation and liquefaction of sands. *J Geotech Eng* 1974;100: 1180–4. <https://doi.org/10.1061/AJGEB6.0000117>.
- Cundall PA, Strack ODL. A discrete numerical model for granular assemblies. *Geotechnique* 1979;29:47–65. <https://doi.org/10.1680/GEOT.1979.29.1.47>.
- Jiang M, Zhao T, Wang X. DEM modelling of cone penetration tests in lunar soil. *Granul Matter* 2021;24:5. <https://doi.org/10.1007/s10035-021-01142-1>.
- Jiang M, Zhang A, Shen Z. Granular soils: from DEM simulation to constitutive modeling. *Acta Geotech* 2020;15:1723–44. <https://doi.org/10.1007/s11440-020-00951-7>.
- Yang X-T, Zhou Y-G, Ma Q, Chen Y-M. Effects of fabric anisotropy on the small-strain shear modulus of granular materials. *Acta Geotech* 2024;20:131–48. <https://doi.org/10.1007/s11440-024-02381-1>.
- Zhou X-H, Zhou Y-G, Chen Y-M. DEM analysis of undrained cyclic behavior and resistance of saturated dense sand without stress reversals. *Granul Matter* 2023;25: 36. <https://doi.org/10.1007/s10035-023-01328-9>.
- Wang R, Fu P, Zhang JM, Dafalias YF. Fabric characteristics and processes influencing the liquefaction and re-liquefaction of sand. *Soil Dynam Earthq Eng* 2019;125:105720. <https://doi.org/10.1016/j.soildyn.2019.105720>.
- Huang X, O'Sullivan C, Hanley KJ, Kwok CY. Partition of the contact force network obtained in discrete element simulations of element tests. *Comput Times Part Mech* 2017;4:145–52. <https://doi.org/10.1007/S40571-015-0095-Y>.
- Ye B, Xie X, Zhao T, Song S, Ma Z, Feng X, et al. Centrifuge tests of macroscopic and mesoscopic investigation into effects of seismic histories on sand liquefaction resistance. *J Earthq Eng* 2022;26:4302–24. <https://doi.org/10.1080/13632469.2020.1826373>.
- Ni X, Ma J, Zhang F. Mechanism of the variation in axial strain of sand subjected to undrained cyclic triaxial loading explained by DEM with non-spherical particles.

- Comput Geotech 2024;165:105846. <https://doi.org/10.1016/J.COMPGEO.2023.105846>.
- [51] Liu G, Rong G, Peng J, Zhou C. Numerical simulation on undrained triaxial behavior of saturated soil by a fluid coupled-DEM model. Eng Geol 2015;193: 256–66. <https://doi.org/10.1016/J.ENGGEOL.2015.04.019>.
- [52] Dubujet P, Dedecker F. Micro-mechanical analysis and modelling of granular materials loaded at constant volume. Granul Matter 1998;1:129–36. <https://doi.org/10.1007/s100350050018>.
- [53] Ai J, Chen JF, Rotter JM, Ooi JY. Assessment of rolling resistance models in discrete element simulations. Powder Technol 2011;206:269–82. <https://doi.org/10.1016/J.POWTEC.2010.09.030>.
- [54] Iwashita K, Oda M. Rolling resistance at contacts in simulation of shear band development by DEM. J Eng Mech 1998;124:285–92.
- [55] Yu P, Liu Y. Dispersion of particle spin waves in granular materials: micromorphic modeling and DEM simulation. Comput Geotech 2025;179:106988. <https://doi.org/10.1016/J.COMPGEO.2024.106988>.
- [56] Dou X, Liu Z, Yang D, Zhao Y, Li Y, Gao D, et al. 3D CFD-DEM modeling of sand production and reservoir compaction in gas hydrate-bearing sediments with gravel packing well completion. Comput Geotech 2025;177:106870. <https://doi.org/10.1016/J.COMPGEO.2024.106870>.
- [57] Zhong H, Zhu Z, Zhao J, Wei L, Zhang Y, Li J, et al. Influence of fine content and mean diameter ratio on the minimum and maximum void ratios of sand–fine mixtures: a discrete element method study. Buildings 2024;14:2877. <https://doi.org/10.3390/buildings14092877>.
- [58] Toki S, Tatsuoka F, Miura S, Yoshimi Y, Yasuda S, Makihara Y. Cyclic undrained triaxial strength of sand by a cooperative test program. Soils Found 1986;26: 117–28. <https://doi.org/10.3208/SANDF1972.26.3.117>.
- [59] Nong ZZ, Park SS, Lee DE. Comparison of sand liquefaction in cyclic triaxial and simple shear tests. Soils Found 2021;61:1071–85. <https://doi.org/10.1016/J.SANDF.2021.05.002>.
- [60] Satake M. Fabric tensor in granular materials. 1982.
- [61] Dafalias YF, Manzari MT. Simple plasticity sand model accounting for fabric change effects. J Eng Mech 2004;130:622–34. [https://doi.org/10.1061/\(ASCE\)0733-9399\(2004\)130:6\(622\)](https://doi.org/10.1061/(ASCE)0733-9399(2004)130:6(622)).
- [62] Sassa S, Sekiguchi H. Analysis of wave-induced liquefaction of sand beds. Geotechnique 2001;51:115–26. <https://doi.org/10.1680/geot.2001.51.2.115>.
- [63] Zhu J-F, Zhao H-Y, Jeng D-S. Effects of principal stress rotation on wave-induced soil response in a poro-elastoplastic sandy seabed. Acta Geotech 2019;14:1717–39. <https://doi.org/10.1007/s11440-019-00809-7>.
- [64] Zhao H-Y, Zhu J-F, Zheng J-H, Zhang J-S. Numerical modelling of the fluid–seabed-structure interactions considering the impact of principal stress axes rotations. Soil Dynam Earthq Eng 2020;136:106242. <https://doi.org/10.1016/j.soildyn.2020.106242>.